*mathematics*

MDPI

*Article*

# Study of Steam-Induced Convection in a Rotating Vertical Flow Channel

**Mohammed Zwawi [1,*], Afrasyab Khan [2], Ali Bahadar [3] and Mohammed Algarni [1]**

[1] Department of Mechanical Engineering, King Abdulaziz University, Rabigh 21911, Saudi Arabia
[2] Research Institute of Mechanical Engineering, Department of Vibration Testing and Equipment Condition Monitoring, South Ural State University, Lenin Prospect 76, 454080 Chelyabinsk, Russia
[3] Department of Chemical and Materials Engineering, King Abdulaziz University, Rabigh 21911, Saudi Arabia
* Correspondence: mzwawi@kau.edu.sa

**Abstract:** The phenomenon of steam–water direct contact condensation has significance in a wide range of industrial applications. Superheated steam was injected upward into a cylindrical water vessel. Visual observations were conducted on a turbulent steam jet to determine the dimensionless steam jet length compared to the steam nozzle exit diameter and the steam maximum swelling ratio as a function of steam mass flux at the nozzle exit, with a gas steam flux ranging from 295–883 kg/m$^2$s. The Reynolds number based on the steam jet's maximum expansion ranged from 41,000 to 93,000. Farther above of the condensation region, the jet evolved as a single-phase heated plume, surrounded by ambient water. Mean axial central velocity profiles were determined against the steam mass flux ranging from 295–883 kg/m$^2$s to observe the exponential drop in the mean axial velocity as the vertical distance increased. The radial velocity distribution within the spread of the jet was determined to be self-similar, and the radial distribution of the velocity profile followed the Gaussian function, after the proper scaling of the vertical distance and the axial mean velocity.

**Keywords:** DCC steam injection; single-phase thermal plume; mean axial velocity; plume Richardson number

**MSC:** 76B10

check for updates

**Citation:** Zwawi, M.; Khan, A.; Bahadar, A.; Algarni, M. Study of Steam-Induced Convection in a Rotating Vertical Flow Channel. *Mathematics* **2023**, *11*, 79. https://doi.org/10.3390/math11010079

Academic Editors: Mohsen Sharifpur, Josua P. Meyer and S. Suseel Jai Krishnan

Received: 20 November 2022
Revised: 13 December 2022
Accepted: 19 December 2022
Published: 25 December 2022



## 1. Introduction

There have been numerous processes (e.g., combustion, nuclear, etc.) involving the injection of steam into liquid (e.g., water), with the main purpose of obtaining high heat and mass transfer rates owing to the direct contact between the phases of the same fluid or different fluids. Such processes are operated at varying conditions, leading or not leading to complete phase transformation [1]. For instance, steam originates from the orifices into the water, with ensuing heat transport into the water surrounding the steam. However, the transfer of heat to the remote locations within a column relies mainly on flow-induced mixing and dilution. The consequence of an injection of a fluid into a sufficiently large tank containing a motionless fluid is a jet, which is highlighted by a mean velocity characterized by an axisymmetric distribution of self-preserving velocity [2–4]. However, inducing saturated or superheated vapors into the liquid led to the formation of condensing jets, which has been proven valuable towards achieving high mixing and heating rates [5]. The self-preservation of the velocity profiles in the case of non-condensing jets has been broadly investigated, focusing on a region apart from a point source [6–12]. However, over the span of last 25 years, the velocity distribution of the jets in the vicinity of the exit of the fluid nozzle, as well as the far field have been analyzed [11,13,14]. In these studies, the perception of self-similarity in the away field of the jets was analyzed in relation to the mean axial velocity profiles and the resulting turbulence of the jets. The concept of scaling the parameter of self-similarity at a distance farther from jet's origin depends on the effective radius of the spread of the jet when the bulk density of the jet farther away from the exit is the same as the mass flux and the momentum flux of the jet at the exit [2,10,15].

There are many investigations regarding saturated and superheated steam injection into the water (e.g., [16–24], in which a strong entrainment and part dissipation of the axial momentum occurs in the consolidated condensation of the steam jet and within the interface between the steam and the surrounding liquid. However, a single-phase thermal liquid jet remains farther from the condensation region. Studies involving an upward steam injection into the confined pool of water provided information on the steam jet-induced mean velocity distribution, as well as the turbulence [3,19,25–27]. The turbulence associated with the steam jet, as well as the continuation of the condensed single-phase jet at upward distances far removed from the exit, is vital for the usefulness of the flow and the thermal mixing in the pool, as related to the safety aspects of the nuclear reactor, which are directly linked to the combined elements of the steam imitated turbulent jet [19,28]. The studies used a pitot tube to measure the velocity profiles of the turbulent jet and extracted mixing details associated with the steam injection. However, Hussein et al. [7] applied a PIV technique to determine the features of the steam jet, including the mean velocity and turbulent properties, whereas Choo et. al. [19] used PIV to characterize the flow and mixing of the steam using upward and downward injections in a confined pool of water. They extracted the velocity profiles of the single-phase jet at different upstream distances from the PIV velocity vectors.

The experimental work conducted thus far in the field of the direct contact condensation of a steam jet driven, horizontally or vertically, into subcooled water is summarized in Table 1. The details provided here involve both geometrical (i.e., steam orientation, nozzle diameter, and column size) and operating (i.e., steam mass flux, water subcooling temperature) conditions, as well as flow regimes observed in these experimental works.

**Table 1.** Condensation regimes and experimental parameters for steam injected into subcooled water.

| Investigations | Injector Diameter (mm) | Injector Exit Orientation | Steam Mass Flux (kg/m$^2$s) or Flowrate (g/s) | Water Subcooling (°C) | Flow Regimes |
|---|---|---|---|---|---|
| [29] | 0.4–9.5 | Horizontal injection | 332–2050 | 28–79 | Vapor cavity |
| [3] | 4.45–10.85 | Horizontal, vertical, L = 0.12 m | 330–550 kg/m$^2$s | 17-82 | SC-IOC *, CO-BCO * |
| [4] | 5 | Vertical upward | <1.6 g/s, 1.6–6.1 g/s | 16.5 | Discreet bubbling transition to unstable axisymmetric jet |
| [5] | 1.6 | Vertical upward | 15–22 cm/s bubble rise velocity | 15–100 | Bubbling, bubble oscillation, bubble collapse at pressures > 10.3 bars |
| [6] | 3.0 | Vertical upward, $z_0 = 0$ | Steam inlet pressure: 0.3 MPa (T = 135 °C) | 25–60 | Turbulent steam jet, followed by thermally stratified plume |
| [7] | 2.2 and 3.0 | Horizontal | 298–723 | 20–70 | Supersonic jet |
| [8] | 50.8 | Horizontal | 17.8 *, 20 and 50 g/s * 0.5% air mass fraction | 60–66 | Bubbling turbulent jet |
| [9] | 2.5 | Vertical upward and vertical downward | 300.28–650.77 | 30–60 | Turbulent jet (vertical up) and pool mixing (vertical down) |

**Table 1.** *Cont.*

| Investigations | Injector Diameter (mm) | Injector Exit Orientation | Steam Mass Flux (kg/m$^2$s) or Flowrate (g/s) | Water Subcooling (°C) | Flow Regimes |
|---|---|---|---|---|---|
| [10] | 8 | Vertical upward | 150–500 (water rate 0.14–6.65 kg/s) | 20–70 | Hemispherical, conical, ellipsoidal, cylindrical, divergent steam plume |
| [11] | 6 and 8 | Vertical upward | 8.34–50.13 | 40–85 | Bubble regime |

* SC: Stable condensation, CO: Condensation oscillation, IOC: Interfacial oscillation condensation, BCO: Bubbling condensation oscillation.

## 2. Equipment and Instrumentation

### *2.1. Experimental Setup*

The experimental setup is illustrated in Figure 1. As seen in this Figure 1, the experimental setup consisted of a cylindrical column of 12 cm in diameter and 1 m in height. The column was made of Perspex, and its thickness was 2 mm. The Perspex cylinder contained a nozzle (id 6 mm) inserted through a bottom stainless-steel plate. The nozzle was constructed from stainless steel, with an inner adiabatic coating to avoid condensation along the inner surface of the nozzle. As illustrated in Table 2, the steam was injected at absolute pressure extending from 3 to 8.5 bars to deliver steam at 295 kg/m$^2$s to 883 kg/m$^2$s, whereas the temperature of the subcooled water in the column was held at 25–50 °C (i.e., 298–323 K) respectively. Lip seals were installed covering the joint between the column base and the nozzle, as well as between the column and the steel plate, to prevent leakage from the column base. Among the two ports installed on the divergent section of the nozzle, one port was used to mount the temperature sensor (K-type thermocouple), and the other port housed the pressure sensor to measure the pressure at the approximate location inside the nozzle exit. Stale steam was acquired from an electric steam generator (Type K-DH, Electric Steam Generator AB & Co, Copenhagen, Denmark, flow rate = 5–270 kg/h) at 2–10 bars, (working pressure = 2–8.5 bars). A vortex steam flowmeter was utilized with the steam flowmeter, exhibiting about 0.75% accuracy.

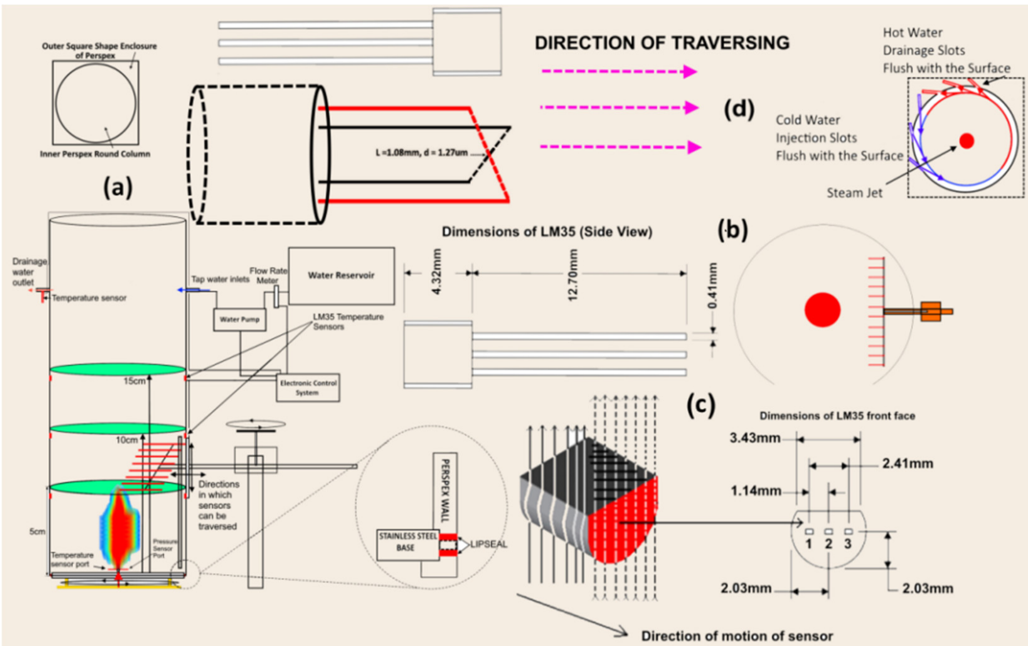


**Figure 1.** *Cont.*

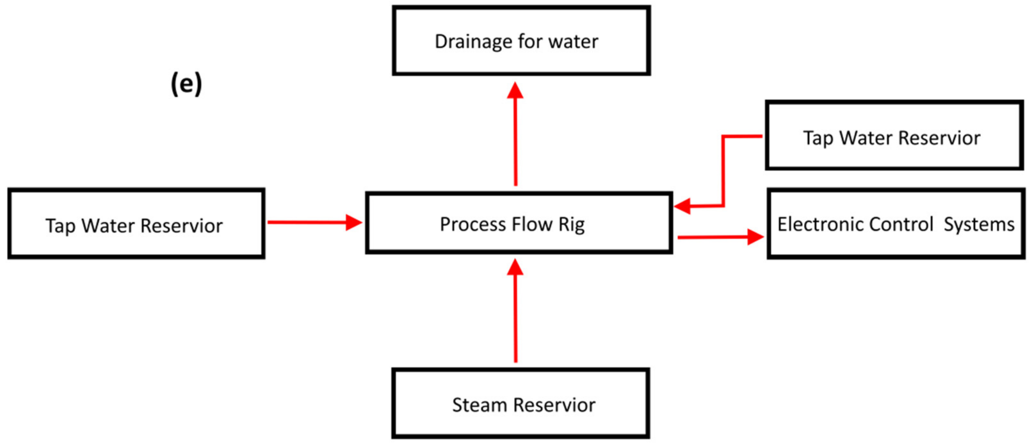


**Figure 1.** (**a**) Schematic of an experimental setup and (**b**–**d**) the geometrical arrangements of the sensors used; (**e**) the schematic flow diagram.

**Table 2.** Experimental operating conditions.

| Parameters | Operating Range |
|---|---|
| Steam inlet absolute pressure $p_s$ (bars) | 3.0–8.5 |
| Steam mass flux at nozzle exit $G_e$ (kg/m$^2$s) | 295–883 |
| Ambient pressure at submerged nozzle exit $p_a$ (bars) | 1.07–1.073 |
| Water temperature $T_f$ °C (K) | 25–50 (298–323) |
| Submerged height of nozzle exits $h_{sub}$ (m) | 0.61 |
| Vessel inner diameter (m) | 0.12 |
| Nozzle exit diameter $d_e$ (m) | 0.006 |

The remixing of the hot water from the top into the lower region of the column was prevented by the use of 5 inlet ports and 5 outlet (drainage) ports/ducts, which were located at a height of 20 cm from the base of the column. The inner diameter of each of these ducts was 20 mm, due to the lip seal-based joint with the column, provided through the stainless-steel enclosure ring inhibiting the lip seal, as seen in Figure 1. The direction of the injection of the cold water and the drainage of the hot/warm water through the 10 top-mounted ducts is along the periphery of the inner column wall. In this way, the cold water was introduced into the column in the form of circulating currents. The outlet ducts were also aligned with the curved body of the inner surface of the walls of the column, as shown in Figure 1. The 5 drainage ducts were joined together into a single pipe. A temperature sensor was mounted on this pipe, which was used for measuring the temperature of the drained water to control the amount of the injected water using an 89C51 micro-controller-based electronic control system (ECS) by adjusting the amount of the injected tap water at a temperature value from the subcooled range using a servo motor. The constant drainage of the hot water from the top was assured by draining the warm water from the top. In addition, 6 temperature sensors were mounted to the inner body of the column at the heights (h) of 0.2–2.5, 5, 10, 15, 20, 30, 40, 50, and 60 cm from the exit of the nozzle. These 6 temperature sensors were also connected to the ECS, which helped to automate the injection of the tap water into the column. The flow rate of the cooling water injected from the top varied between 0.001–0.0032 L/s.

### *2.2. PIV Technique*

A PIV unit, along with a camera (Megaplus ES1.0, Kodak/Roper Scientific/USA) having a resolution 2048 × 2048~7.4 μm$^2$ in each pixel, was used to measure the pointwise fluid velocity in the present experimental investigations. The laser exhibited a pulse frequency of ~15 Hz and a power 200 mJ/pulse, with a national electronics data acquisition and data processing software module. Polyamide particles of 50 µm in diameter and a density of 1.03 $kg/m^3$ were chosen to illuminate the flow, as their density was nearly the same as that of the water. A laser sheet of 2 mm thickness was initially directed on the column in three horizontal positions; whereas afterwards, PIV was used to obtain the velocity cross-sectional scans at different heights, i.e., h = 0–100 mm, 100–200 mm, 200–300 mm, and 300–400 mm from the nozzle exit, and a high speed camera (Megaplus ES1.0, Kodak/Roper Scientific/USA) was positioned in accordance to the measurement slice to capture the images of the steam jet or the plume. All the raw data were processed through the data acquisition consisting of an A/D converter and the PC. The measurements were obtained at a rate of 10 Hz for a duration of 600 s, which was equivalent to ~6000 frames.

The CCD camera was tuned in such a way that it could adjust each of the frames in focusing the region that met the regional focus of the plan at the desired height from the nozzle's exit. Any irregularity found in the obtained PIV frames was removed through detection analysis. The precise measurement related to the magnification of the laser pulse, as well as the separation between the pulses, was linked to perform the calibration of the PIV system, and the pulse separation was estimated by guiding the laser sheet onto the photodetector, which was connected to the oscilloscope. This indicated the extent of separation with respect to the distance between the point of the laser emergence and its incidence on the photodetector. The errors associated with the magnification were estimated by focusing the laser sheet on a given dimensional grid and comparing the ratio of the given grid spacing with the known grid spacing. This guided the determination of the range of the optical distortions. In cases where there was no distortion, the value of the ratio did not vary at any of the heights along the fluid domain. The uncertainties associated with the measurements are within 0.1–0.3%. The significant geometrical details of the experimental setup, including the nozzle dimensions and the range of the operating parameters, are summarized in Table 2.

Each of the lasers was exposed in a synchronized fashion for a duration of 0.1 s. The water was held at the desired temperature in a range of 25–50 °C, with a gap of 5 °C between the two adjacent cases. The largest difference between the water temperature at the mid-section of the column and the top of the column was 4.85 °C. For instance, within 13 min from the onset of the steam injection, the top surface of the column could achieve the temperature of 25 °C. Subsequent to the remaining phases of the experiments, simultaneous measurements for temperature and velocity were collected to compute the influence of the condensation potential and the measurement of the momentum on the engulfment and entrainment. The distance between the two sensors was maintained at about 2.5 cm to prevent the influence of the hot wire on the temperature being measured by the LM35 temperature sensor.

## 3. Empirical Correlations and Physical Analysis

### *3.1. Vertical Upward Injection of Steam into a Pool of Subcooled Water*

#### 3.1.1. Overall Jet/Plume Layout

A schematic of a steam jet escaping out of the nozzle's exit into the subcooled water, followed by steam condensation and the development of a single-phase thermal water plume, along with the creation of self-preserving regions of a thermal plume, can be seen in Figure 2. A complete picture of the steam plume surrounded by the subcooled water is based on visual observations, as well as the PIV measurements of the upward steam injection into the pool of water, which was studied extensively [2,3,17,19] by and others. Steam exits from the nozzle into the pool of water as an intense jet. The inside of the jet is filled with steam, and the outer boundary is an interface between the steam and the water [20]. The steam's jet exhibits a swollen portion at some distance downstream of the nozzle exit, and subsequently, the jet narrows down as the rapid contraction towards the middle line sets in, and this continues to a point where the jet breaks into two phases:

steam and water. This region has been referred to as the development region of a thermal single-phase plume, which spreads radially as it propagates upward due to its buoyancy.

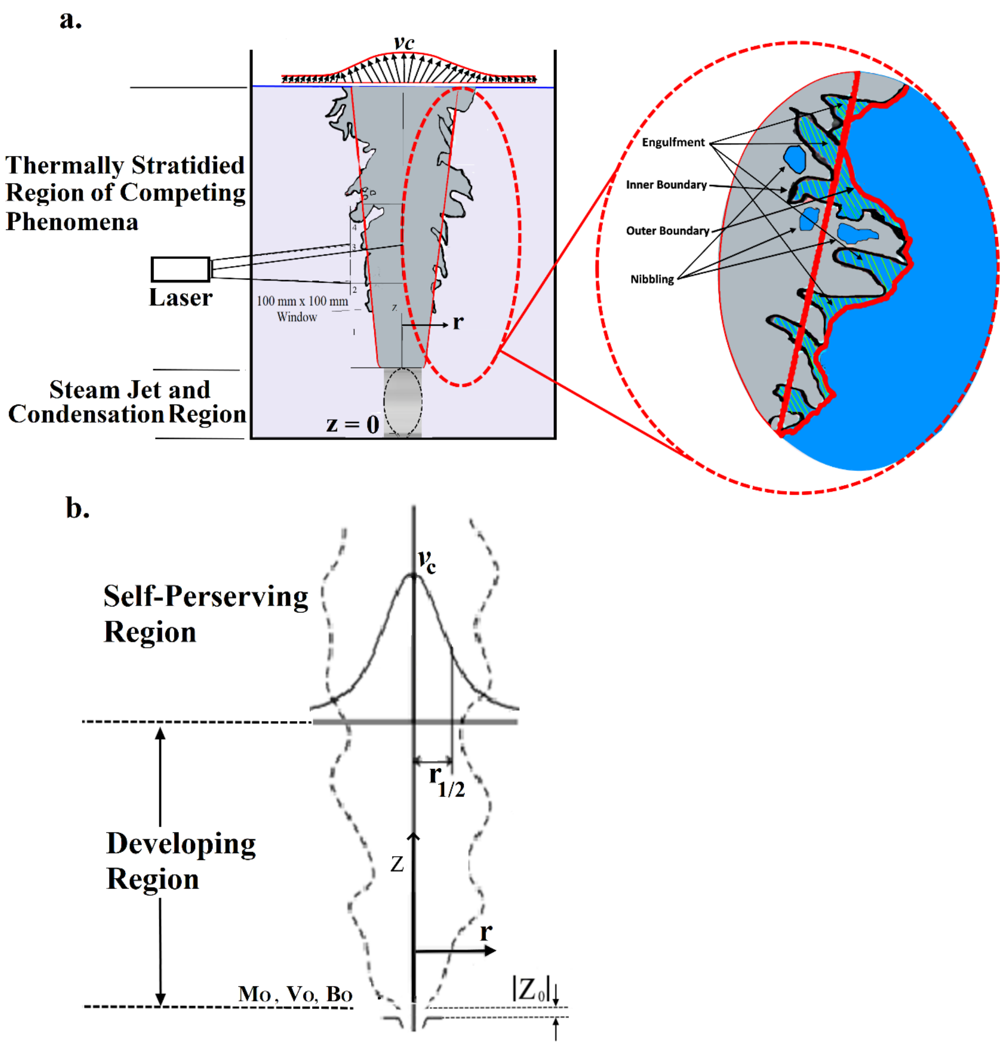


**Figure 2.** (**a**) A schematic of overall steam jet and its single-phase plume regions; (**b**) a schematic of developing and developed regions of a single-phase liquid heated plume.

The steam jet close to the nozzle exit region resembles an onion-like shape, with most of the swelling in the middle, and constricted lower and upper regions. This can be achieved through realization of the momentum balance. In a segment near the exit of the steam nozzle, there is an obvious element of radial momentum. However, the existence of the steam–water interface acts to entrain the water surrounding the steam inside, and the mass conservation contributes towards deflecting the steam outward [30]. In the present situation, however, the dominance of condensation within the steam–water interface acts to further decrease the interface. Moreover, the contribution of the buoyancy to the shaping of the steam jet's profile cannot be ruled out.

At a short distance from the onion-shape region of the steam jet, a little-developed section can be seen in Figure 2a. With the use of PIV measurements, this region was described as a condensed steam jet [26]. However, further downstream of this region, the sustained thermal profile, owing to the competing forces associated with the momentum, the radial entrainment of the outside layer of the plume with the surrounding water can be noted, and to some extent, buoyancy also contributes to this profile. Further, the interaction of the large-scale interfacial instabilities with the surrounding water is characterized as entrainment, whereas the dissipation of the small-scale eddies is defined as the engulfment.

3.1.2. Overall Jet/Plume Layout

Based on their experimental data, Kerney et. al. [28] proposed a correlation for the penetration of vapor jets ($L_j$) into the subcooled liquid, which was validated for upward steam injection into the subcooled water. The correlation is expressed as:

$$\frac{L_j}{d_e} = 0.2588{B_C}^{-1}\sqrt{\frac{G_e}{G_m}} \quad (1)$$

where $B_C$ is the condensation potential, which was defined by [17] as:

$$B_C = \frac{h_{fs} - h_\alpha}{h_e - h_{fs}} \quad (2)$$

where $h_{fs}$ is the enthalpy of saturated liquid, $h_\alpha$ is the enthalpy of the liquid at ambient condition, and $h_e$ is the steam enthalpy at the nozzle exit. Moreover, [13] also found an empirical correlation for steam jet penetration into the subcooled liquid, which was based on the steam mass flux (applicable at $G_e > 200$ kg/m$^2$s) and the condensation potential, expressed as

$$\frac{L_j}{d_e} = 0.5923{B_C}^{-0.66}\left(\frac{G_e}{G_m}\right)^{0.3444} \quad (3)$$

The subscripts e and m represent the values of $G$ at the nozzle exit and the jet's mean value, respectively, and $B_C$ can alternatively be expressed as:

$$B_C = \frac{c_{p,f}(T_s - T_f)}{h_{fg}} \quad (4)$$

where $c_{p,f}$ is the liquid specific heat (j/kg. °C), and $h_{fg}$ is the latent heat of vaporization (j/kg). Kim et. al. [31] found that their data for steam jet length correlated to the following relationship:

$$\frac{L_j}{d_e} = 0.503{B_C}^{-0.70127}\left(\frac{G_e}{G_m}\right)^{0.47688} \quad (5)$$

Another empirical correlation was suggested by [21] for a supersonic steam injection into the pool of water, expressed as:

$$\frac{L_j}{d} = 0.868{B_C}^{-0.6}\left(\frac{p_s}{p_a}\right)\left(\frac{G_e}{G_m}\right)^{0.5} \quad (6)$$

where $p_s$ and $p_a$ are the pressure of inlet steam and the pressure of the ambient water. This correlation was found to be more accurate than others at higher water temperatures, as other correlations predicted an overestimation of the penetration length, whereas the use of the steam pressure in the correlation provides a similar effect to restrict this overestimation.

3.1.3. Steam Condensation

It can be seen from Figure 2 that the outer layer of the steam jet interacts with the subcooled water, and this transforms steam into water due to the occurrence of condensation. Model relationships related to the phase change [15] were used to compute the steam's mass rate, which was transformed to the water. The transformation of the phase change was realized by the model through the application of heat transfer between the vapor and liquid phases, which is authentic in cases of the condensation or evaporation of pure substances. Therefore, the sensible heat flux (j/m$^2$) across the vapor–liquid interface to the individual phases can be expressed as:

$$q_f = h_f(T_i - T_f) \quad (7)$$

$$q_s = h_s(T_i - T_s) \quad (8)$$

where $h_f$ and $h_s$ are the heat transfer coefficients (j/m$^2$K) for water and steam, respectively, and $T_i$, $T_f$, and $T_s$ are the temperatures (K) of the interface, the water, and the steam, respectively. Moreover, Equation (7) provides an estimation of transfer of heat from the interface to the water phase, and Equation (8) provides an estimation of the transfer of heat from the interface to the steam. The heat transfer coefficient between the interface and the steam phase was estimated by following the complete heat transfer across the interface. This emphasized the application of a simple heat balance to estimate the heat flux. However, the heat transfer coefficient between the interface and the water ($h_f$) was estimated by using Ranz–Marshall equation [16], written as:

$$Nu = 2 + 0.6Re^{0.6}Pr^{0.3} \tag{9}$$

where $Nu$ is the Nusselt number, $Re$ is the Reynolds number, and $Pr$ is the Prandtl number; these are expressed as:

$$Nu = \frac{h_f d_e}{K_f}\ ;\ R_e = \frac{d_e v_s}{\nu_f};\ P_r = \frac{C_{pf}\mu_f}{K_f} \tag{10}$$

where $d_e$ is the nozzle exit diameter, $h_f$ is the water's heat transfer coefficient, $K_f$ is the water thermal conductivity (W/mK), $v_s$ is the steam axial velocity at the nozzle exit, $\nu_f$ is the kinematic viscosity of the liquid (m$^2$/s), $C_{pf}$ is the specific heat of the liquid, j/kgK, $\mu_f$ is the dynamic viscosity of the liquid, and kg/ms, $K_f$ is the thermal conductivity of liquid. The interfacial temperature, $T_i$ can be evaluated by considering thermodynamic equilibrium, which was assumed to be the same for both phases (i.e., saturation temperature). Therefore, the exchange of mass between the vapor and the liquid can be determined from the overall heat balance, which is expressed as:

$$Q_s = q_s - \dot{m}_{sf}H_{si} \tag{11}$$

$$Q_f = q_f + \dot{m}_{sf}H_{fi} \tag{12}$$

where $\dot{m}_{sf}$ represents the mass flux being transferred from the vapor phase into the liquid phase, and $H_{si}$ and $H_{fi}$ symbolize the interfacial heat enthalpy based on the difference between the inward and outward elements of the vapor and water phases due to the conversion of the phase. The interphase mass flux can then be expressed as:

$$\dot{m}_{sf} = \frac{q_f + q_s}{H_{si} - H_{fi}} \tag{13}$$

where $H_{si}$ denotes the steam specific enthalpy, and $H_{fi}$ is the specific enthalpy of water at interfacial temperature $T_{sat}$, which are regarded as the interfacial values of enthalpy carried in and out of the phases due to phase change. Thus, Equation (11) is re-written by incorporating the correction to the volumetric steam rate, Q (m$^3$/s), due to the steam's condensation rate ($\dot{m}_{sf}$), which is expressed as:

$$Q = \frac{\dot{m}_s - \dot{m}_{sf}}{\rho_s} \tag{14}$$

## 4. Results and Discussion

### *4.1. Steam Jet Length to Diameter Ratio ($L_j/d_e$)*

The length of the steam jet or plume is referred to as the axial length region containing the steam phase only. Visual observations and high-speed photography were used to obtain the steam jet length. This method is not useful when the temperature of the water is close the boiling temperature because in such cases, it is difficult to detect the precise interface between the steam and the surrounding water. However, this technique is appropriate in the present case, where the maximum temperature of the subcooled water is 50 °C.

The measured values of the steam jet length ($L_j$), normalized by the inner diameter of the steam nozzle's exit, are presented in Figure 3 as a function of the steam mass flux at the nozzle exit and the subcooled water temperature. The normalized steam jet length is found to increase with an increase in the steam mass flux and the water temperature. However, for all steam mass fluxes, the slope of the normalized steam jet length is slightly higher than the values obtained at lower temperatures of subcooled water. This is due to the fact that driving mechanism of condensation reduces because of the decrease in the driving parameter of the temperature difference resulting from the increase in the subcooled water temperature. The overall range of the values of the dimensionless steam jet length is 1.7–6.2.

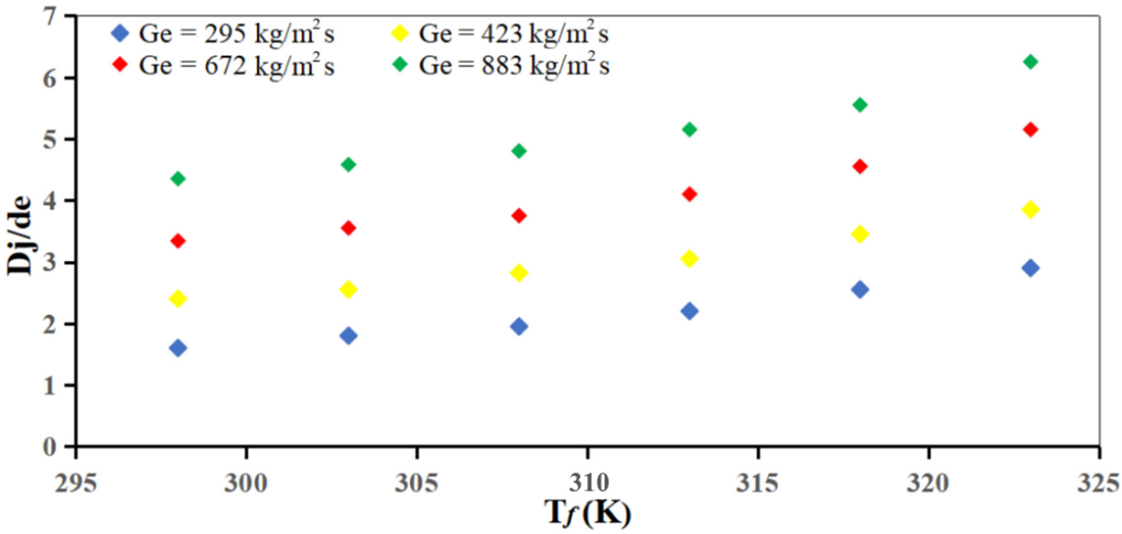


**Figure 3.** Relationship of the steam jet length to the nozzle exit diameter as a function of the subcooled water temperature.

There have been many investigations (i.e., [2,10,13,17–19] and others) which measured the steam jet length for higher steam mass fluxes, i.e., ≥200 kg/m$^2$s. Figure 4 presents the correlations between the measured dimensionless steam jet length proposed by [2,13,20,21] compared with the measured values obtained for the steam mass flux of Ge = 672 kg/m$^2$s. As seen from the Figure 4, the correlation of [21], associated with the supersonic steam injection, was not appropriate for the sonic and subsonic steam jet condensation. Moreover, our measurements were found to follow the correlation proposed by [2], when compared to the measurements in the other studies.

Maximum Swelling of the Steam Jet

The ratios of the maximum swelling of the steam jet to the inner diameter of the steam nozzle exit ($D_{jmax}/d_e$) under different steam mass flux levels at the nozzle exit (Ge) and varying subcooled water temperatures are presented in Figure 5. The radial growth of steam increases with increase in both steam mass flux and the subcooled water temperature. The maximum radial expansion of the steam in the present work was noted in the range of 1.075–1.49, as seen in the Table 3. The highest value of the ratio in our case is much smaller than the ratios determined by [14,22] because they conducted measurements at much higher steam mass fluxes, and the temperature range of the water in these works exceeded that of the water used in the present study. However, the trend of the $D_{jmax}/d_e$ in the present case has been found to be consistent with that exhibited in these investigations, within the operating range of steam mass flux and water temperature utilized in the present work. However, the maximum expansion of the steam jet in the case of [21] is higher than that in our study, due to the wider range of subcooled water temperatures operated by the authors.

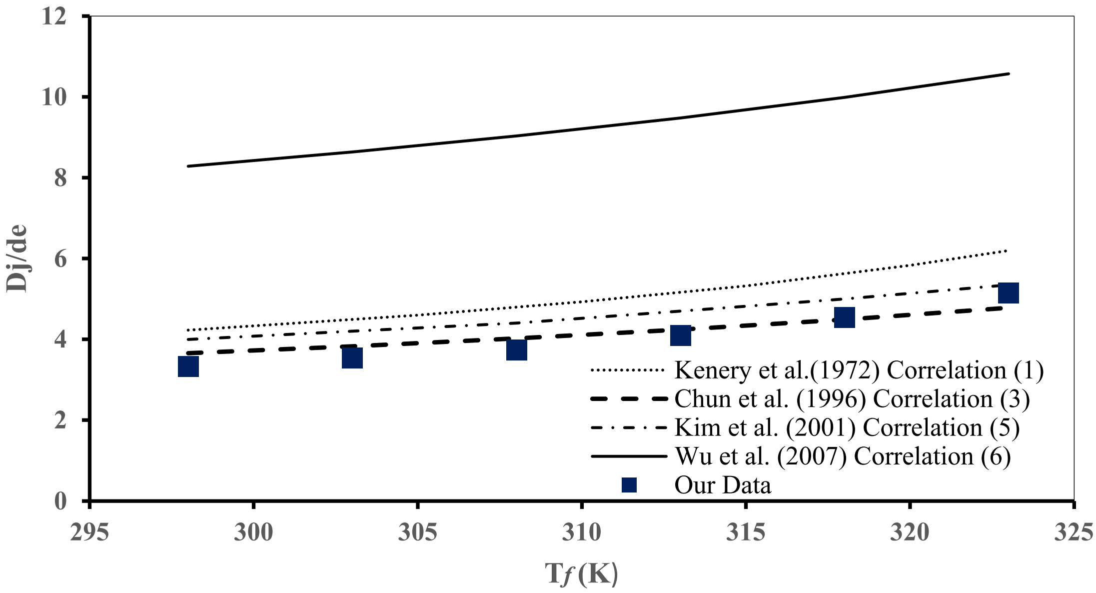


**Figure 4.** Correlations with the present data for dimensionless steam jet length for the steam mass flux of Ge = 672 kg/m$^2$s.

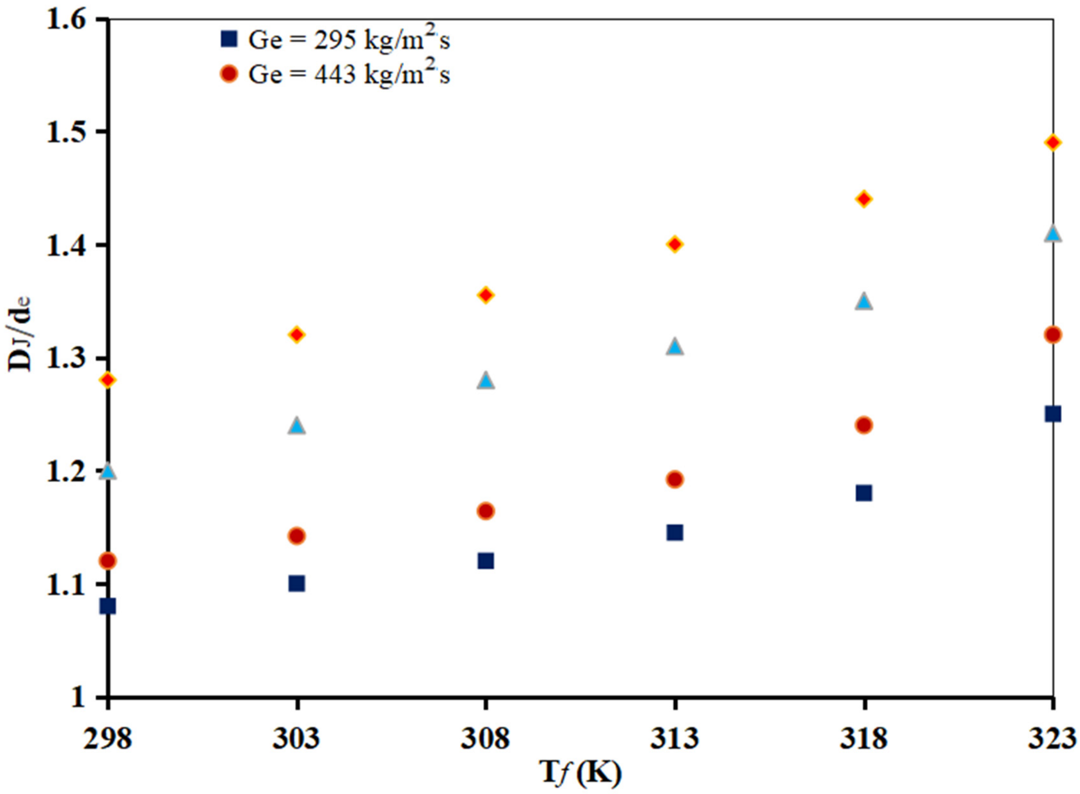


**Figure 5.** Maximum swelling ratio compared with subcooled water temperature.

**Table 3.** Maximum swelling ratio.

| Investigation | Ge (kg/m$^2$s) | Subcooled Water Temperature (K) | Max Swelling Ratio ($D_{jmax}/d_e$) |
|---|---|---|---|
| Chun et al. (1996) [18] | 200–1500 | 293–343 | 1.0–2.3 |
| Kim et al. (2005) [27] | 250–1188 | 293–343 | 1.05–2.3 |

**Table 3.** *Cont.*

| Investigation | Ge (kg/m$^2$s) | Subcooled Water Temperature (K) | Max Swelling Ratio ($D_{jmax}/d_e$) |
|---|---|---|---|
| Wu et al. (2007) [20] | 298–723 | 293–343 | 1.08–1.95 |
| Our Values | 295–883 | 298–323 | 1.075–1.49 |

### 4.2. Single Phase Thermal Plume

#### 4.2.1. Mean Axial Velocity

The mean of the axial velocity of the single-phase thermal plume in case of Ge = 295 kg/m$^2$s and Ge = 672 kg/m$^2$s are presented in Figure 6a,b, and their normalized profiles can be seen in Figure 7a,b. The plume is determined to interact and entrain the surrounding water due to its having inherent eddying qualities. The mean axial velocity measurements display obvious profiles with a maximum value at the mid-point of the column, and the profile decreases to nearly zero value, which is observed at the plume's outside boundary; this is the margin between the thermal water plume and the surrounding ambient water.

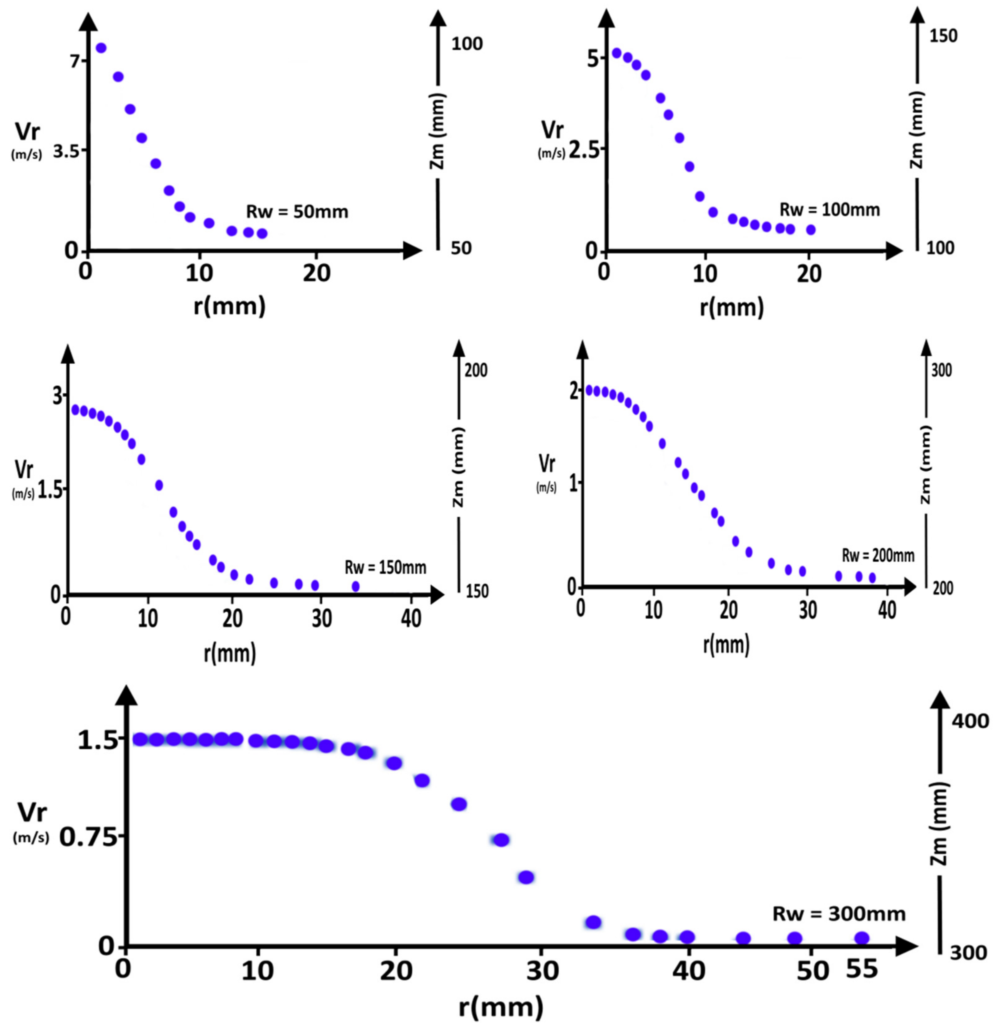


(**a**)

**Figure 6.** *Cont.*

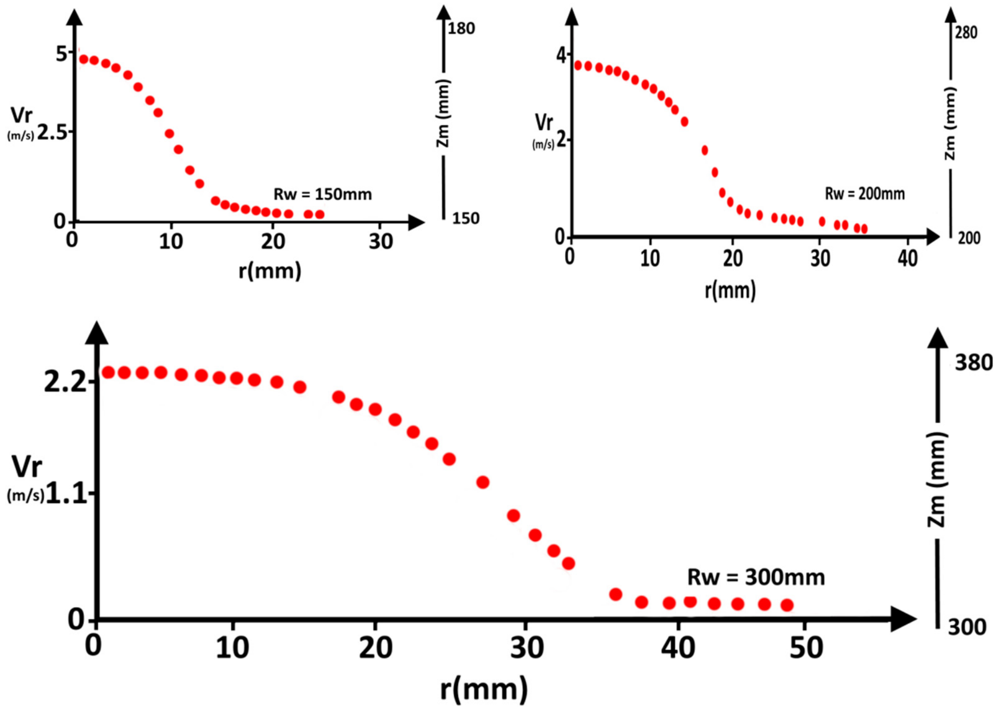


(**b**)

**Figure 6.** (**a**) Mean axial velocity at G = 295 kg/m$^2$s and T = 50 °C. (**b**) Mean axial velocity at G = 672 kg/m$^2$s and T = 50 °C.

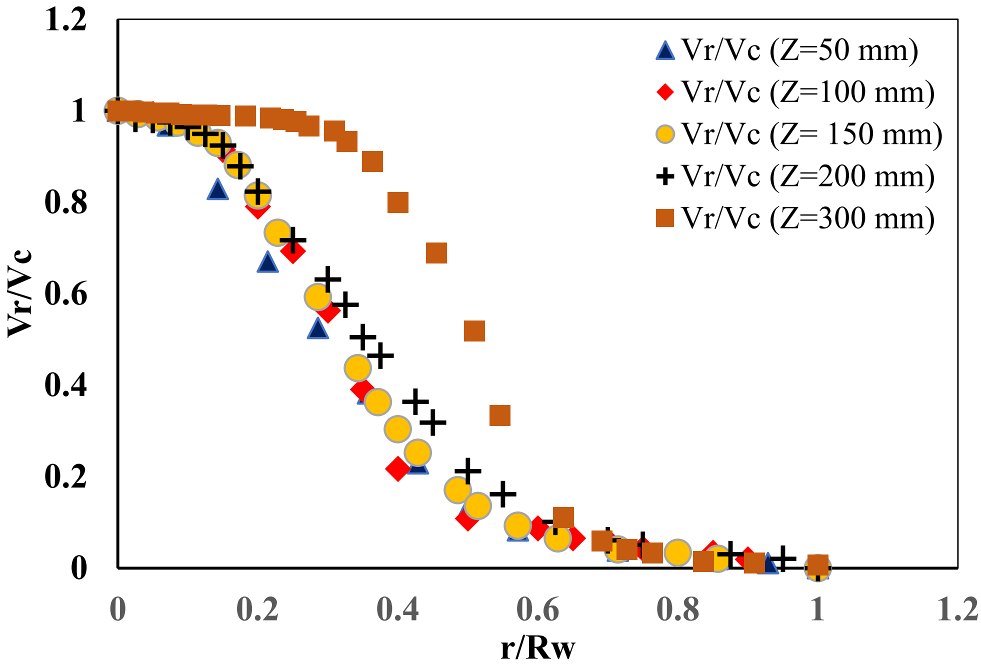


(a)

**Figure 7.** *Cont.*

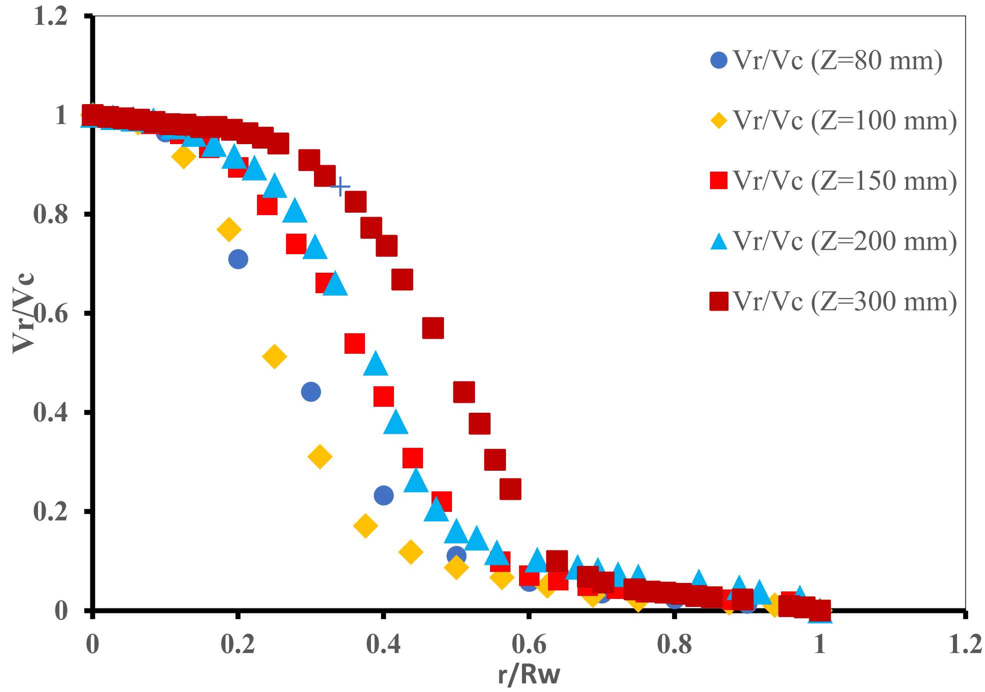


(**b**)

**Figure 7.** (**a**). Normalized axial velocity compared with normalized radial distance of the water jet at ***Ge*** = 295 kg/m$^2$s. (**b**) Normalized axial velocity compared with normalized radial distance of the water jet at ***Ge*** = 672 kg/m$^2$s.

### 4.2.2. Mean velocity Profiles along the Vertical Height

Figure 6a,b reveals the mean axial velocity profiles, which were measured at a steam mass flux of 295 kg/m$^2$s and 672 kg/m$^2$s, respectively. These figures indicate a visible difference between the crosswise layer as the steam mass flux varies. In the case of a higher steam mass flux, the condensed steam plume requires more time to transverse the distance leading to stabilization. Moreover, the height developed by increasing the steam mass flux is higher than the height development with a lower steam mass flux. The dimensionless mean velocity profiles vs. the dimensionless radial distances indicate a shifting of the mean velocity profile towards the right as the plume's layer spreads in a vertical distance. This shows that the stabilizing influence of the plume decreases with the downstream distance due to the weakening of the shear across the interface of the plume.

### 4.2.3. Self-Similarity

The significance behind self-similarity is used to demonstrate that the flow attains a dynamic equilibrium due to the matching of the mean values with the higher-order moments [32]. Typically, self-similar variables depend on the conditional scale, and they subsequently validate a generalized characteristic in a region, which indicates a fully established flow. Thus, the mean value of the condensed steam velocity in the middle of the plume $\{\mathbf{i.e.,\ v_c(z) = v(z,0),}\}$ and the plume's width (i.e., $\boldsymbol{r}$) may be outlined as two characteristic scales, and $\eta\{= \frac{r}{z-z_0},\ \boldsymbol{z_0}$ **is the virtual origin**$\}$ is an alternative dimensionless scale for determining the cross-stream magnitude. Measurements of the single-phase turbulent jets show that at far fields, $v_c$ is inversely proportional to the axial distance and is expressed as:

$$v_c = \frac{C}{z-z_0} \tag{15}$$

where $\boldsymbol{C}$ is a coefficient associated to the mean center line velocity [33]. Both $\boldsymbol{C}$ and $\boldsymbol{z_0}$ can be determined from the measured values of the central velocity of the single-phase turbulent jet, Figure 8, and they are strongly dependent on steam mass flux, $\boldsymbol{G}$. Values of $z_0$ and $C$ as a function of $\boldsymbol{G}$ and pool temperature can be seen in Table 4.

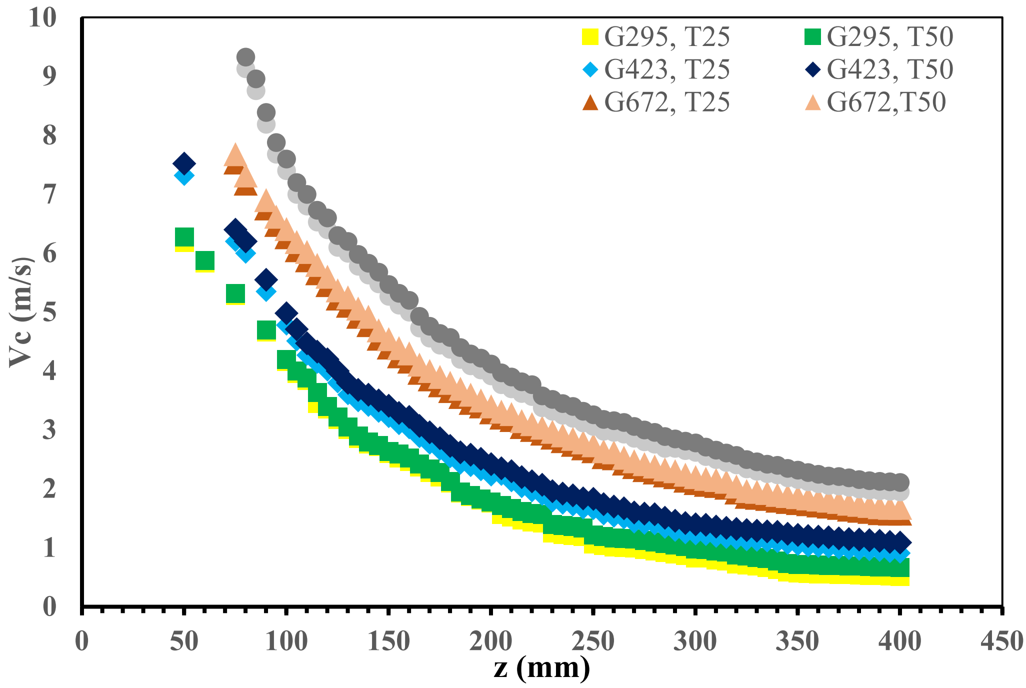


**Figure 8.** Centerline velocity along the height from the condensation point.

**Table 4.** Turbulent flow self-similarity parameters.

| Exp. Case | $C$ (m$^2$/s) | $z_0$ (m) | $S$ |
|---|---|---|---|
| G295T25 | 0.653–0.672 | −0.042 to −0.0453 | 0.0887 |
| G295T50 | 0.691–0.707 | −0.037 to −0.042 | 0.0893 |
| G423T25 | 0.863–0.893 | −0.0343 to −0.0392 | 0.0907 |
| G423T50 | 0.897–0.924 | −0.0303 to −0.0327 | 0.0917 |
| G672T25 | 1.223–1.38 | −0.0281 to −0.0305 | 0.0936 |
| G672T50 | 1.254–1.423 | −0.023 to −0.024 | 0.0957 |
| G883T25 | 1.412–1.632 | −0.0235 to −0.0253 | 0.0953 |
| G883T50 | 1.453–1.493 | −0.0197 to −0.0213 | 0.0973 |

An analogous feature of a turbulent jet was highlighted by Hussain et al. (1994) [7], who exhibited that nearly all values of the mean vertical velocity of a single-phase jet are represented by a Gaussian profile expressed as:

$$\frac{v}{v_c} = e^{-S\eta^2} \tag{16}$$

where $\boldsymbol{S}$ is a coefficient to signify the curvature of a mean velocity profile, which can be obtained from the single-phase jet velocity measurements and the $v_z/v_c$ profile, in the case of $\boldsymbol{G}$ = 672 kg/m$^2$s and a subcooled water temperature of 50 °C, as seen in Figure 9. The spreading rate of the jet, $S$, is expressed as:

$$S = \frac{r_{\frac{1}{2}}(z)}{z - z_0} \tag{17}$$

where $\boldsymbol{r}_{\frac{1}{2}}(z)$ represents radial distance, where the mean vertical velocity reduces to half of the jet's centerline velocity, and $\boldsymbol{U_C}$ $(z)$ is at a corresponding vertical distance $\boldsymbol{z}$ from the condensation region. The jet plume's spread is estimated from the measured axial velocity profiles (Figure 9). Thus, $\boldsymbol{S}$, with its dependence on the steam mass flux ($\boldsymbol{G_S}$), can be seen in Table 4. The value of virtual origin is negative, in the present case, whereas the value of $z_0$, in case of non-condensing single-phase jets, is positive [33]. In fact, the value of $z_0$ depends on the origin of the jet, and in the present case, water is formed by the conversion of steam's jet at the nozzle's exit, whose shape and dimensions depend on the steam's mass flux and the temperature of the pool water. The spreading rate constant $\boldsymbol{S}$, in the present case, lies between 0.0887–0.0973 against the steam mass flux that ranges from 295 kg/m$^2$s to 883 kg/m$^2$s, respectively, against the pool water temperature of 25 °C and 50 °C. These results have been found to be in agreement with those for the condensing jets, as determined by and, where $\boldsymbol{S}$ ranged from 0.09–0.098. Our values for $\boldsymbol{S}$ agree with the measurements in, wherein the research obtained 0.094 for $\boldsymbol{S}$ in air axisymmetric jets. Our values are also in agreement with the measurements obtained for a water jet by [30].

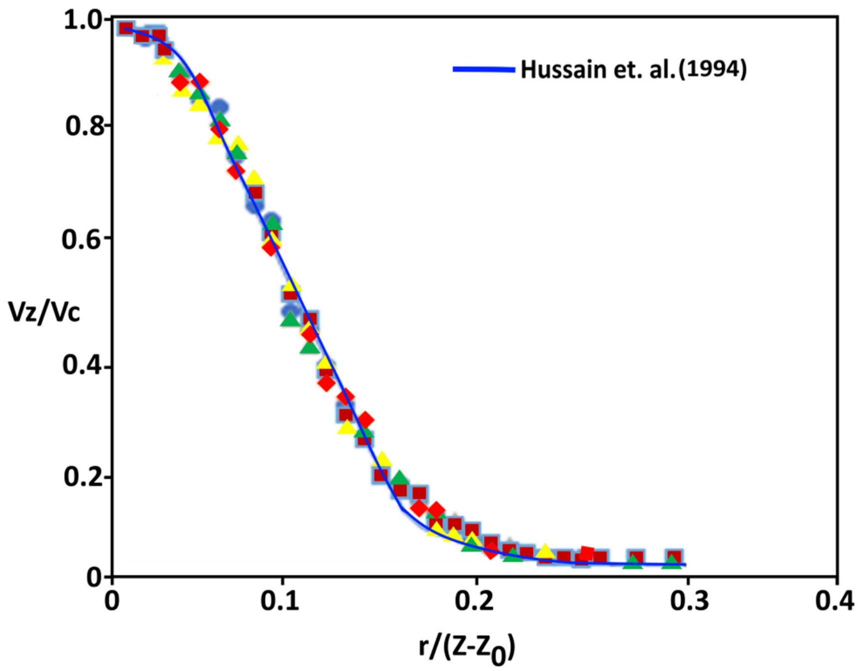


**Figure 9.** Self-preserved mean axial velocity profile across the width of the plume.

### 4.3. Vertical Steam Submerged Injection in Pool of Water

The steam injection into a pool of subcooled water shows a buoyant jetting regime [20,34]. Generally, a region within a pool can be classified into the following: a pure buoyant plume, a pure momentum jet, and a combination of the two extreme cases. A pure jet is something that possesses a dominant contribution from the momentum to sustain it, while there is no contribution from buoyancy. However, the tangential shear acting across the interface between the steam and the subcooled water of the jet tends toward the occurrence of the Kelvin–Helmholtz (KH) instabilities [30,31,35,36]. The KH instability gives rise to the formation and evolution of vortices, which results in a turbulent mixing layer between the steam–water interface and the surrounding water. The KH instabilities can contribute towards increasing the surface area available for heat transfer between the jet and the surrounding water.

A forced plume is liable to become condensed as it comes into contact with the surrounding subcooled water. This presents a case where the transition between the two extremes occurs. Here, buoyancy tends to stratify the pool, whereas momentum acts to unify the pool. Thus, under the competing influence between the momentum and the buoyancy fluxes, it is possible to move from a stratified to a mixed case. Increased mixing between the vapor and the liquid phases causes an enhanced heat transfer between the two phases.

In the case of high flow steam injection (e.g., supersonic) through a nozzle at submerged depths, condensation can occur over a short distance [37,38], if the pool is sufficiently subcooled (e.g., <50 °C). This can lead to a variable balance between buoyancy and inertia along the jet plume trajectory, where it can be defined by variable transition properties consisting of a buoyant condensing vapor upstream, followed by a hot liquid turbulent jet downstream.

Radial Growth of a Liquid Thermal Jet

Measurements were made along the vertical axis ranging from 50 to 400 mm above the source against the steam mass flux of 295 kg/m$^2$s and 672 kg/m$^2$s at a pool water temperature of 50 °C. Figure 10 shows the evolution of the normalized radius ($\boldsymbol{R_v/R_o}$) of the single-phase jet against the normalized vertical height ($z/D_o$) from the condensation region. It can be observed that the thermal liquid jet tends to spread linearly with the height in the development of the far field region of the jet; however, the trend becomes vertical after crossing $\boldsymbol{z/Ro} \approx 50$. The values of radial growth for the two conditions are clearly different as the jets spread, as seen in the case where $\boldsymbol{G_e}$ = 295 kg/m$^2$s is larger than in the case of $\boldsymbol{G_e}$ = 672 kg/m$^2$s (see Figure 10), which induces the slope of the trend for $\boldsymbol{G_e}$ = 295 kg/m$^2$s, which is is slightly higher than that of the $\boldsymbol{G_e}$ = 672 kg/m$^2$s. The trend of the radial growth profiles in the present case agrees with that of the heated air jet exerted into ambient air [39]. However, the slope of their data is considerably higher, owing to the considerably weaker turbulent dissipation in their case than in ours.

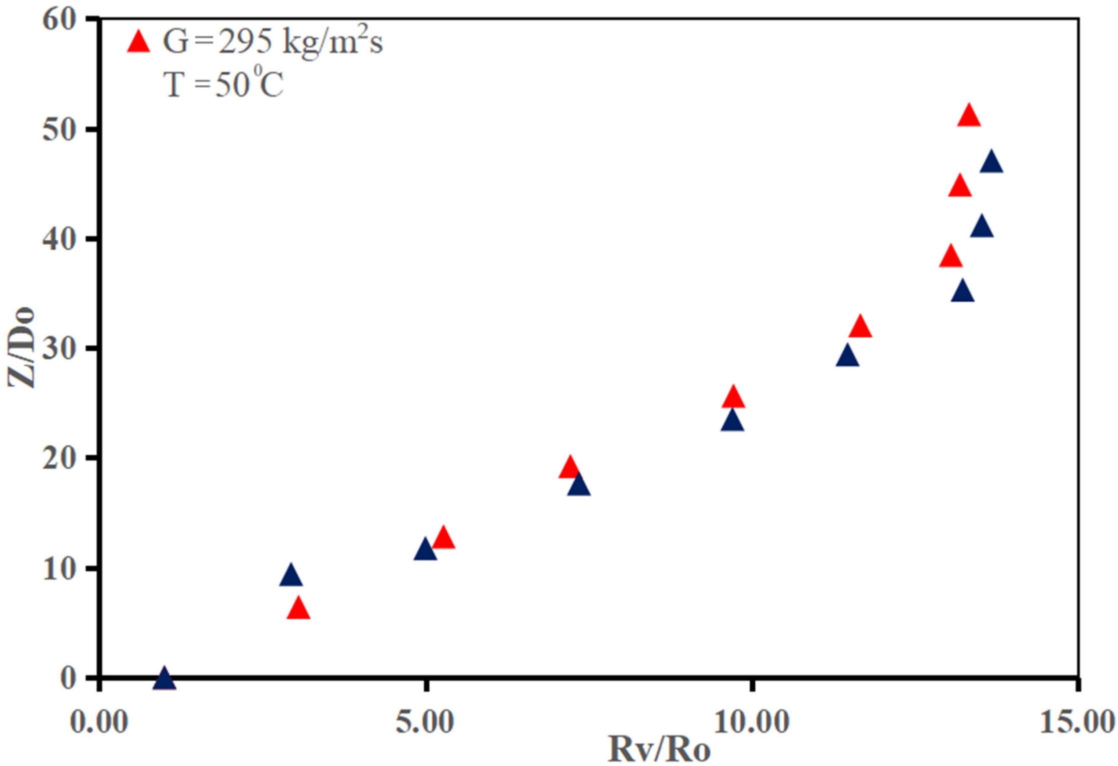


**Figure 10.** Normalized radial growth of a thermal liquid jet compared to the normalized vertical distance.

## 5. Conclusions

When the steam is injected vertically upward into the column filled with subcooled water, the consequence result in the formation of three regions: a steam jet region involving condensation, a developing jet region, and a self-sustained single-phase plume having a virtual origin ($z_0$) within a range of 2–4 de from the real injection point. The significant outcomes of the work are listed as follows:

a. The condensation of the steam jet submerged in the subcooled water supports the measurements, which show that with increase in steam mass flux and water temperatures ranging from 295–883 kg/m$^2$s and 25–50 °C, respectively, the normalized the steam jet length, as well as the maximum swelling ratio, which were in the range 1.7–6.2 and 1.075–1.49, respectively. The normalized steam jet length compared to the steam mass flux of 672 kg/m$^2$s and 50 °C was found to be in agreement with the correlation suggested by Kerney et al. (1972) [28].
b. The PIV measurements of the axial mean velocity at a steam mass flux of 295 kg/m$^2$s and 672 kg/m$^2$s were obtained at different downstream locations of the single-phase turbulent plume, which exhibits consolidated self-similar features of the plume in an axisymmetric shape, including the constants used to determine the plume's shape.
c. The mean axial velocity profiles of the thermal water plume support self-similarity, with the spreading of the velocity profiles being similar to the non-condensed single-phase jets occurring at the similar Reynolds numbers.

**Author Contributions:** M.Z.: Conceptualization, Funding acquisition, Resources, Writing; A.K.: Supervision, Methodology, Data curation, Writing—Original draft preparation. A.B.: Visualization, Writing—Reviewing and Editing. M.A.: Software, Validation. All authors have read and agreed to the published version of the manuscript.

**Funding:** The authors extend their appreciation to the Deputyship for Research and Innovation, Ministry of Education in Saudi Arabia for funding this research work through the project number (IFPHI-029-829-2020) and King Abdulaziz University, DSR, Jeddah, Saudi Arabia.

**Data Availability Statement:** Not Applicable.

**Conflicts of Interest:** The authors declare no conflict of interest.

## References

1. Sideman, S. Direct Contact Heat Transfer between Immiscible Liquids. In *Advances in Chemical Engineering*; Elsevier: Amsterdam, The Netherlands, 1966; Volume 6, pp. 207–286. ISBN 0065-2377.
2. Van Wissen, R.J.; Schreel, K.R.; Van Der Geld, C.W. Particle Image Velocimetry Measurements of a Steam-Driven Confined Turbulent Water Jet. *J. Fluid Mech.* **2005**, *530*, 353–368. [CrossRef]
3. Norman, T.L.; Revankar, S.T. Jet-Plume Condensation of Steam–Air Mixtures in Subcooled Water, Part 1: Experiments. *Nucl. Eng. Des.* **2010**, *240*, 524–532. [CrossRef]
4. Meng, Z.; Zhang, W.; Liu, J.; Yan, R.; Shen, G. Experimental Study on the Condensation of Sonic Steam in the Underwater Environment. *Nucl. Eng. Technol.* **2019**, *51*, 987–995. [CrossRef]
5. Jo, B.; Erkan, N.; Okamoto, K. Richardson Number Criteria for Direct-Contact-Condensation-Induced Thermal Stratification Using Visualization. *Prog. Nucl. Energy* **2020**, *118*, 103095. [CrossRef]
6. Panchapakesan, N.R.; Lumley, J.L. Turbulence Measurements in Axisymmetric Jets of Air and Helium. Part 1. Air Jet. *J. Fluid Mech.* **1993**, *246*, 197–223. [CrossRef]
7. Hussein, H.J.; Capp, S.P.; George, W.K. Velocity Measurements in a High-Reynolds-Number, Momentum-Conserving, Axisymmetric, Turbulent Jet. *J. Fluid Mech.* **1994**, *258*, 31–75. [CrossRef]
8. Fellouah, H.; Ball, C.G.; Pollard, A. Reynolds Number Effects within the Development Region of a Turbulent Round Free Jet. *Int. J. Heat Mass Transf.* **2009**, *52*, 3943–3954. [CrossRef]
9. Mi, J.; Kalt, P.; Nathan, G.; Wong, C. PIV Measurements of a Turbulent Jet Issuing from Round Sharp-Edged Plate. *Exp. Fluids* **2007**, *42*, 625–637. [CrossRef]
10. Wolf, M.; Lüthi, B.; Holzner, M.; Krug, D.; Kinzelbach, W.; Tsinober, A. Investigations on the Local Entrainment Velocity in a Turbulent Jet. *Phys. Fluids* **2012**, *24*, 105110. [CrossRef]
11. Monin, A.S.; Yaglom, A.M. *Statistical Fluid Mechanics, Volume II: Mechanics of Turbulence*; Courier Corporation: Chelmsford, MA, USA, 2013; Volume 2, ISBN 0-486-31814-1.
12. Pope, S.B. Turbulent Flows. *Meas. Sci. Technol.* **2001**, *12*, 2020–2021. [CrossRef]
13. George, W.K. The Self-Preservation of Turbulent Flows and Its Relation to Initial Conditions and Coherent Structures. *Adv. Turbul.* **1989**, *3973*.

14. Salizzoni, P.; Hunt, G.R.; A L I Z Z O N I 2 A N D, P.S. Dynamical Variability of Axisymmetric Buoyant Plumes Managing Air for Green Inner Cities (MAGIC) View Project Optimisation of Smoke Control in Tunnels View Project Dynamical Variability of Axisymmetric Buoyant Plumes. *Artic. J. Fluid Mech.* **2015**. [CrossRef]
15. Mistry, D.; Philip, J.; Dawson, J.R.; Marusic, I. Entrainment at Multi-Scales across the Turbulent/Non-Turbulent Interface in an Axisymmetric Jet. *J. Fluid Mech.* **2016**, *802*, 690–725. [CrossRef]
16. Weimer, J.; Faeth, G.; Olson, D. Penetration of Vapor Jets Submerged in Subcooled Liquids. *AIChE J.* **1973**, *19*, 552–558. [CrossRef]
17. Chen, L.D.; Faeth, G.M. Condensation of Submerged Vapor Jets in Subcooled Liquids. *J. Heat Transf.* **1982**, *104*, 774–780. [CrossRef]
18. Chun, M.H.; Kim, Y.S.; Park, J.W. An Investigation of Direct Condensation of Steam Jet in Subcooled Water. *Int. Commun. Heat Mass Transf.* **1996**, *23*, 947–958. [CrossRef]
19. Choo, Y.J.; Song, C.-H. PIV Measurements of Turbulent Jet and Pool Mixing Produced by a Steam Jet Discharge in a Subcooled Water Pool. *Nucl. Eng. Des.* **2010**, *240*, 2215–2224. [CrossRef]
20. Wu, X.-Z.; Yan, J.-J.; Shao, S.-F.; Cao, Y.; Liu, J.-P. Experimental Study on the Condensation of Supersonic Steam Jet Submerged in Quiescent Subcooled Water: Steam Plume Shape and Heat Transfer. *Int. J. Multiph. Flow* **2007**, *33*, 1296–1307. [CrossRef]
21. Xu, Q.; Guo, L.; Zou, S.; Chen, J.; Zhang, X. Experimental Study on Direct Contact Condensation of Stable Steam Jet in Water Flow in a Vertical Pipe. *Int. J. Heat Mass Transf.* **2013**, *66*, 808–817. [CrossRef]
22. Khan, A.; Haq, N.U.; Chughtai, I.R.; Shah, A.; Sanaullah, K. Experimental Investigations of the Interface between Steam and Water Two Phase Flows. *Int. J. Heat Mass Transf.* **2014**, *73*, 521–532. [CrossRef]
23. Sanaullah, K.; Khan, A.; Takriff, M.S.; Zen, H.; Shah, A.; Chughtai, I.R.; Jamil, T.; Fong, L.S.; Haq, N.U. Determining Potential of Subcooling to Attenuate Hydrodynamic Instabilities for Steam–Water Two Phase Flow. *Int. J. Heat Mass Transf.* **2015**, *84*, 178–197. [CrossRef]
24. Khan, A.; Takriff, M.S.; Rosli, M.I.; Othman, N.T.A.; Sanaullah, K.; Rigit, A.R.H.; Shah, A.; Ullah, A.; Mushtaq, M.U. Turbulence Dissipation & Its Induced Entrainment in Subsonic Swirling Steam Injected in Cocurrent Flowing Water. *Int. J. Heat Mass Transf.* **2019**, *145*, 118716. [CrossRef]
25. Norman, T.L.; Park, H.-S.; Revankar, S.T.; Ishii, M.; Kelly, J.M. Thermal Stratification and Mixing in an Open Water Pool by Submerged Mixtures of Steam and Air. In *Proceedings of the Energy Conversion and Resources*; ASMEDC: Chicago, IL, USA, 2006; pp. 137–151.
26. Chen, X.; Tian, M.; Qu, X.; Zhang, Y. Numerical Investigation on the Interfacial Characteristics of Steam Jet Condensation in Subcooled Water Flow in a Restricted Channel. *Int. J. Heat Mass Transf.* **2019**, *137*, 908–921. [CrossRef]
27. Kim, Y.S.; Youn, Y.J. Experimental Study of Turbulent Jet Induced by Steam Jet Condensation through a Hole in a Water Tank. *Int. Commun. Heat Mass Transf.* **2008**, *35*, 21–29. [CrossRef]
28. Kerney, P.J.; Faeth, G.M.; Olson, D.R. Penetration Characteristics of a Submerged Steam Jet. *AIChE J.* **1972**, *18*, 548–553. [CrossRef]
29. Jeje, A.; Asante, B.; Ross, B. Steam Bubbling Regimes and Direct Contact Condensation Heat Transfer in Highly Subcooled Water. *Chem. Eng. Sci.* **1990**, *45*, 639–650. [CrossRef]
30. Gulawani, S.S.; Joshi, J.B.; Shah, M.S.; RamaPrasad, C.S.; Shukla, D.S. CFD Analysis of Flow Pattern and Heat Transfer in Direct Contact Steam Condensation. *Chem. Eng. Sci.* **2006**, *61*, 5204–5220. [CrossRef]
31. Kim, H.Y.; Bae, Y.Y.; Song, C.H.; Park, J.K.; Choi, S.M. Experimental Study on Stable Steam Condensation in a Quenching Tank. *Int. J. Energy Res.* **2001**, *25*, 239–252. [CrossRef]
32. Khan, A.; Sanaullah, K.; Takriff, M.S.; Zen, H.; Fong, L.S. Inclined Injection of Supersonic Steam into Subcooled Water: A CFD Analysis. *Adv. Mater. Res.* **2013**, *845*, 101–107. [CrossRef]
33. Khan, A.; Sanaullah, K.; Takriff, M.S.; Zen, H.; Rigit, A.R.H.; Shah, A.; Chughtai, I.R.; Jamil, T. Pressure Stresses Generated Due to Supersonic Steam Jet Induced Hydrodynamic Instabilities. *Chem. Eng. Sci.* **2016**, *146*, 44–63. [CrossRef]
34. Jirka, G.H.; Harleman, D.R.F. Stability and Mixing of a Vertical Plane Buoyant Jet in Confined Depth. *J. Fluid Mech.* **1979**, *94*, 275–304. [CrossRef]
35. Qiu, B.; Yang, Q.; Meng, F.; Zhang, D.; Chong, D.; Liu, J.; Yan, J. Experimental Investigation on the Interface Shape of Bubble Condensation for Vertical Upward Steam Jet at Low Mass Flux. *Int. J. Heat Mass Transf.* **2020**, *157*, 119909. [CrossRef]
36. Khan, A.; Sanaullah, K.; Ghazwani, H.A.S.; Ullah, A.; Rigit, A.R.H. Buoyancy Effects on the Supersonic Steam Jet Injection into Cocurrently and Countercurrently Flowing Water. *Arch. Appl. Mech.* **2021**, *91*, 3125–3149. [CrossRef]
37. Kuz, V.A. Evaporation of Small Drops. *J. Appl. Phys.* **1991**, *69*, 7034–7036. [CrossRef]
38. Simpson, M.E.; Chan, C.K. Hydrodynamics of a Subsonic Vapor Jet in Subcooled Liquid. *J. Heat Transf.* **1982**, *104*, 271–278. [CrossRef]
39. Townsend, A. *The Structure of Turbulent Shear Flow*; Cambridge University Press: Cambridge, UK, 1980; ISBN 0-521-29819-9.